ChemPubSoc Europe

DOI: 10.1002/open.201500038

Open Access ChemistryOPEN Full Papers

Metal-Organic Chemical Vapor Deposition (MOCVD) Synthesis of Heteroepitaxial $Pr_{0.7}Ca_{0.3}MnO_3$ Films: Effects of Processing Conditions on Structural/Morphological and Functional Properties

Maria R. Catalano,[a] Giuseppe Cucinotta,[b] Emanuela Schilirò,[a] Matteo Mannini,*[b] Andrea Caneschi,[b] Raffaella Lo Nigro,[c] Emanuele Smecca,[a] Guglielmo G. Condorelli,[a] and Graziella Malandrino*[a]

Calcium-doped praseodymium manganite films ($Pr_{0.7}Ca_{0.3}MnO_3$, PCMO) were prepared by metal-organic chemical vapor deposition (MOCVD) on $SrTiO_3$ (001) and $SrTiO_3$ (110) single-crystal substrates. Structural characterization through X-ray diffraction (XRD) measurements and transmission electron microscopy (TEM) analyses confirmed the formation of epitaxial PCMO phase films. Energy dispersive X-ray (EDX) and X-ray photoelectron spectroscopy (XPS) characterization was used to confirm lateral and vertical composition and the purity of the deposited films. Magnetic measurements, obtained in zero-field-cooling (ZFC) and field-cooling (FC) modes, provided evidence of the presence of a ferromagnetic (FM) transition temperature, which was correlated to the transport properties of the film. The functional properties of the deposited films, combined with the structural and chemical characterization collected data, indicate that the MOCVD approach represents a suitable route for the growth of pure, good quality PCMO for the fabrication of novel spintronic devices.

Introduction

Manganite perovskite materials with the general formula $RE_{1-x}A_xMnO_3$ (RE = rare-earth metal, A = bivalent alkaline metal) have been intensively investigated for their electrical and magnetic properties, which are closely related to the complex structure.[1] Through the colossal magnetoresistance (CMR) phenomenon,[2] observed around the ferromagnetic transition temperature (T_c), these materials undergo a dramatic decrease in their resistance (negative magnetoresistance) when an external magnetic field is applied. This property is particularly relevant from a technological point of view since manganite films have been proposed as active components in resistive[3] and magnetic[4] data storage devices as well as in other emerging technologies including spintronics. The richness of properties featuring these materials arises from the coexistence and the interplay of different competitive magnetic states.[5] In particular, the properties of the material are associated with the magnetism of mixed-valence Mn ions and depend on the ratio between Mn^{3+} and Mn^{4+} ions, responsible for the phenomenon of charge ordering (CO) and double-exchange (DE) interaction.[6,7] In addition, the complexity of $Pr_{0.7}Ca_{0.3}MnO_3$ (PCMO) systems arises from anisotropy effects due to the distortion of the MnO_6 octahedral geometry in the perovskite structure as a consequence of the small size of the A-site cations coupled with the Jahn–Teller distortion in Mn^{3+} as well as the cooperative ordering of those ions.

Among the doped manganite perovskites, PCMO stoichiometry has been largely investigated not only for its significant magnetoresistance properties, but also for the recently observed electric-pulse-induced resistance (EPIR),[3,8] an interesting property that could be used in next-generation nonvolatile resistance random access memories[9–12] and semiconductor field effect transistors.[13]

Since all the above-mentioned technological applications require the synthesis of the manganite material in thin film form, the optimization of a straightforward, easily scalable synthetic approach is a crucial issue from an applicative point of view. In this context, metal organic chemical vapor deposition (MOCVD)[14] has proven to be a powerful technique for the fabrication of perovskite systems with complex compositions[15,16]

[a] Dr. M. R. Catalano, E. Schilirò, E. Smecca, Prof. Dr. G. G. Condorelli, Prof. Dr. G. Malandrino
Dipartimento di Scienze Chimiche, Università degli Studi di Catania
INSTM UdR di Catania, 95125 Catania (Italy)
E-mail: gmalandrino@unict.it

[b] G. Cucinotta, Dr. M. Mannini, Prof. Dr. A. Caneschi
Dipartimento di Chimica "Ugo Schiff"
Università degli Studi di Firenze, INSTM UdR di Firenze
Via della Lastruccia 3, 50019 Sesto Fiorentino (FI) (Italy)
E-mail: matteo.mannini@unifi.it

[c] Dr. R. Lo Nigro
Istituto per la Microelettronica e Microsistemi, Institute for Microelectronics and Microsystems, National Research Council (IMM-CNR)
Strada VIII n. 5, 95121 Catania (Italy)

Supporting information for this article is available on the WWW under http://dx.doi.org/10.1002/open.201500038.

and offers all the potential advantages of a reliable and reproducible method for the fast production of films with highly uniform thickness and composition over large areas.

PCMO thin films have been synthesized by various physical methods, such as pulsed laser deposition,[17] molecular beam epitaxy,[18] and magnetron sputtering.[19] Reports are rare on the use of the MOCVD technique for the synthesis of PCMO,[20,21] while this technique has been extensively employed for the fabrication of $La_{1-x}Sr_xMnO_3$ (LSMO) films.[22–28] Since manganese perovskites are extremely sensitive to structural/chemical alteration, the substrate nature plays a crucial role both on the morphology as well as on the transport properties due to substrate-induced strain.[29–31] In fact, the lattice mismatch between the manganite films and the substrate affects magnetic and electrical properties,[32] such as the temperature and field behavior of the resistivity, the ferromagnetic transition temperature (T_c) and the metallic/insulating transition temperature (T_p).

In this work, the calcium-doped praseodymium manganite thin films, $Pr_{0.7}Ca_{0.3}MnO3$, have been grown by MOCVD using a molten mixture consisting of the $Pr(hfa)_3$·diglyme, $Ca(hfa)_2$·tetraglyme and $Mn(tmhd)_3$ (Hhfa = 1,1,1,5,5,5-hexafluoro-2,4-pentanedione; diglyme = bis(2-methoxyethyl)ether, tetraglyme = 2,5,8,11,14-pentaoxapentadecane; Htmhd = 2,2,6,6-tetramethyl-3,5-heptandione) precursors on $SrTiO_3$ (001) and $SrTiO_3$ (110) substrates, hereafter referred to as STO (001) and STO (110), respectively. The present approach, similar to that previously applied for the deposition of LSMO films,[27,28] offers all the potential advantages of a very reliable and reproducible method for the fast production of epitaxial films with an highly uniform thickness and composition over large areas. The functional properties have been analyzed through measurements of magnetization obtained in zero-field-cooling (ZFC) and in field-cooling (FC) modes and through transport measurements, which allowed to establish dependences of conduction properties of the films on temperature and applied magnetic fields.

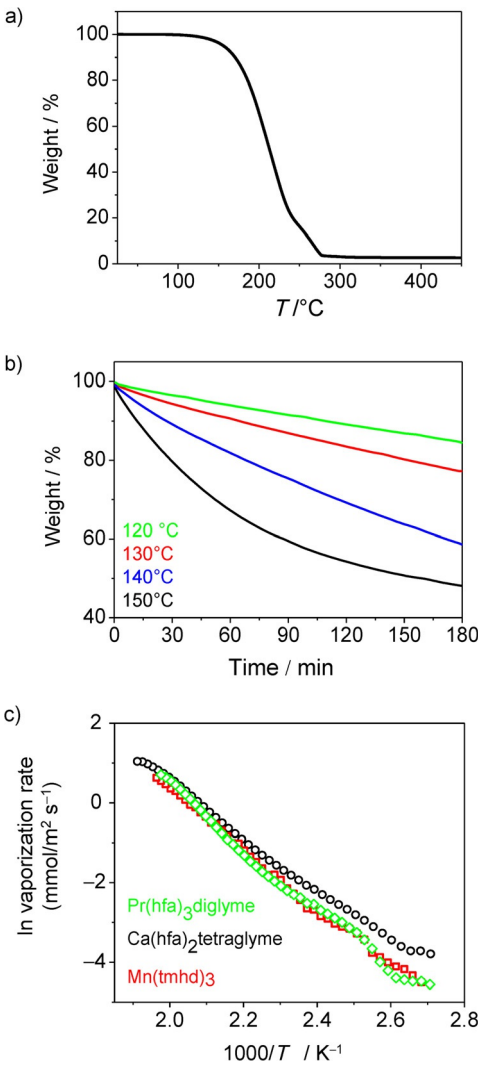

Figure 1. a) Thermogravimetric (TG) and b) isothermal gravimetric curves of the multicomponent Pr:Ca:Mn mixture in the ratio 1.8:0.6:1. c) Vaporization rates of the single Pr, Ca, and Mn precursors.

Results and Discussion

Thermal analysis of the precursor mixture

The multi-element single source consists of a suited mixture of $Pr(hfa)_3$·diglyme, $Ca(hfa)_2$·tetraglyme and $Mn(tmhd)_3$, in an appropriate stoichiometric ratio. The thermal properties of individual precursors have been previously investigated.[33–35] The three adducts are thermally stable, in fact thermogravimetric (TG) analyses indicate that they vaporize intact in a single step with low residues (about 2–3%) left at 350 °C (Figure S1 in the Supporting Information).

Here, a multi-component Pr:Ca:Mn mixture in the ratio 1.8:0.6:1 has been prepared, and a dynamic and isothermal TG characterization has been carried out at atmospheric pressure under purified nitrogen flow. The TG curve (Figure 1a) indicates that the multi-component mixture evaporates quantitatively in the 160–270 °C temperature range, with a 3% residue left at 350 °C, thus indicating that the Pr, Ca, and Mn precursors evaporate simultaneously with a clean process without any side decomposition. A small step may be located at the higher temperature side of the vaporization process, in the 240–270 °C temperature range. This behavior, likely due to slight differences in the vaporization temperature ranges for the three different precursors with the $Ca(hfa)_2$tetraglyme having the highest temperature range (Figure S1 in the Supporting Information), does not represent a problem for the mixture application since the vaporization temperature used in the MOCVD process is much lower, being set at 130 °C. Isothermal thermogravimetric measurements of the mixture (Figure 1b) in the 120–150 °C range for a total duration of 180 min point to a mass loss that is linearly dependent on vaporization time in the range 120–140 °C, excluding secondary phenomena. At the highest temperatures, the observed nonlinear behavior suggests that contributions of individual precursors may prevail, giving rise to differential vaporization rates. The linear fit of the isothermal measurements are reported in Figure S2 in the Supporting Information.

Vaporization rates of the single precursors have been evaluated to relate the composition of the gas phase versus the composition of the precursor mixture (Figure 1c). The almost identical vaporization rates of the three precursors confirm that the gas-phase composition is likely to be similar to the precursor mixture one. This implies that the different composition of the precursor mixture versus the composition of the deposited films is likely to be related to different deposition rates of the three precursors.

Other useful information on the properties of the molten precursor mixture have been obtained through differential scanning calorimetry (DSC) characterization (Figure 2). The

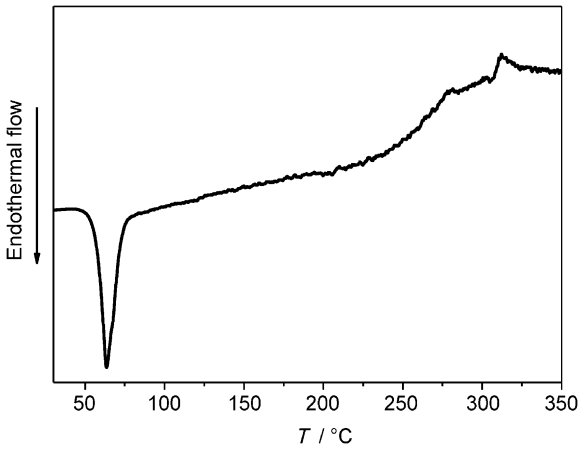

Figure 2. Differential scanning calorimetry (DSC) curve of the multicomponent Pr:Ca:Mn mixture in the ratio 1.8:0.6:1.

molten Pr:Ca:Mn mixture shows an endothermic peak at 63 °C associated with the $Pr(hfa)_3$·diglyme melting (m.p. = 73 °C). No endothermic peaks expected for the $Ca(hfa)_2$·tetraglyme (m.p. = 94 °C) and $Mn(tmhd)_3$ (m.p. = 165 °C) melting points have been observed. Finally a broad endothermic peak in the 200–280 °C temperature range is associated with the mixture vaporization.

Thus, it is likely that the $Pr(hfa)_3$·diglyme precursor acts, on melting, as a solvent for Ca and Mn sources and forms a homogeneous mixture of the three precursors. Note that the absence of any exothermic peak is a confirmation of the mixture thermal stability. From these data, obtained in atmospheric pressure, it is possible to foresee that optimal MOCVD conditions can be achieved under vacuum and to envisage the great advantages of using this procedure depositing PCMO films for practical applications.

Growth and characterization of PCMO films

Several experiments have been carried out to assess the operational parameters, such as deposition temperature, flow of reaction gas (water saturated oxygen flow), ratio of the source mixture to produce good crystalline quality PCMO phase film with the desired stoichiometry. The atomic composition of PCMO thin films has been evaluated through energy dispersive X-ray (EDX) analysis carried out on PCMO films simultaneously deposited on MgO (001) substrate. PCMO films have an almost ideal stoichiometry for a 30% Ca doping, namely Pr:Ca:Mn ratio is $(0.7 \pm 0.05):(0.3 \pm 0.05):(1 \pm 0.05)$. This stoichiometry in the film is obtained when using a Pr:Ca:Mn ratio of 1.8:0.6:1 in the source mixture.

Particular attention has been paid to the effect of substrate orientation on microstructure and morphology of PCMO films. The structural properties of PCMO films have been investigated by using X-ray diffraction (XRD) and transmission electron microscopy (TEM). In the following X-ray and electron diffraction interpretations, the PCMO film signals have been assigned considering a P_{nma} orthorhombic structure,[36] while the STO substrate signals have been assigned as the cubic perovskite structure.[37] The XRD patterns show the formation of the pure phase PCMO films on STO substrates (Figure 3). In particular,

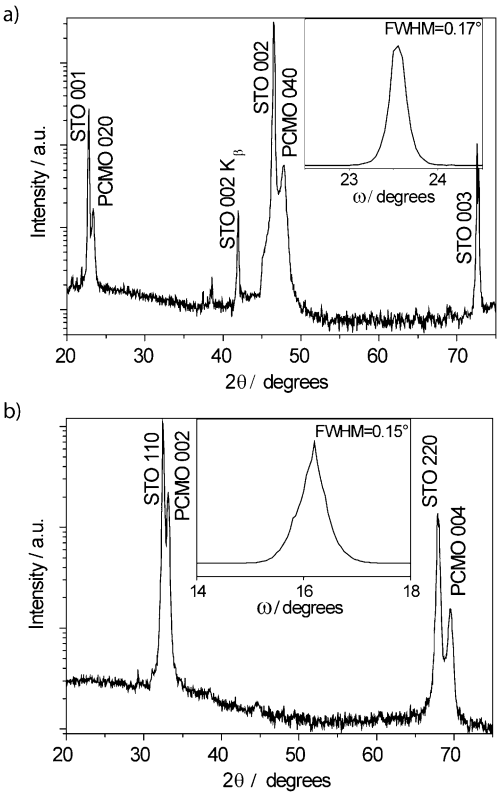

Figure 3. X-ray diffraction (XRD) patterns of PCMO films deposited on a) STO (001) and b) STO (110). Rocking curves of the 040 and 002 reflections are reported in the insets of panels a and b, respectively.

the diffraction pattern of PCMO film deposited on STO (001) is reported in Figure 3a. The peaks at 2θ values of 23.21° and 47.75° can be attributed to 0*k*0 reflections of the PCMO phase, while the STO 001 and 002 reflections are observed at 22.75° and 46.55°, respectively. In Figure 3b, the peak at the 2θ value of 33.15° is assigned to the 002 reflection of the PCMO phase, the one at 69.50° to the 004 reflection, while the peak at 32.45° and 67.85° are due to STO 110 and 220 reflections, respectively. It is worthy to note that no extra peaks are visible even in the log scale of the XRD patterns, thus indicating that no other crystalline impurity phases are present in the films.

The grains dispersion has been determined by ω-scans (rocking curve) of the 040 reflection at 47.75° and of the 002 reflection at 33.15° (insets in Figure 3). The full width at half maximum (FWHM) values of 0.17° and 0.15° for PCMO films deposited on STO (001) and STO (110), respectively, show an excellent out-of-plane alignment of the PCMO films, indicating a high degree of texturing. Additional information regarding the PCMO film epitaxy have been obtained using TEM. TEM image in plane-view of PCMO (010) film grown on STO (001) shows the interference fringes due to dislocations formed at the PCMO/STO interface (Figure 4a). The almost squared imaging of the dislocations is an indication that they are present in both the [100] and [001] plane directions. The presence of dislocations is the most common relaxation effect for epitaxially grown film under mild strain.[38] In Figure 4b, the selected area electron diffraction (SAED) patterns of the PCMO film and STO substrate are shown. Since the two compounds possess very similar plane distances, the spots lying on each circumference showed in the Figure 4b cannot be univocally assigned, but for instance the 3.87 Å distance can be related to (100) STO and to the (101) PCMO plane distances, as well as the 2.75 Å distance can be related to the (110) STO and (002) PCMO plane distances, and finally the 1.95 Å distance has been related to the (200) STO and (202) PCMO plane distances.

In Figure 4b, only the 5.44 Å distance can be certainly assigned to the PCMO. Nevertheless, it is not possible to assign unambiguously this distance to the (100) or (001) plane distances. However, the present electron diffraction pattern provides an important information about the PCMO directions lying on the substrate plane, which certainly are represented by the [100] and [001], while the [010] direction is perpendicular to the substrate plane. This conclusion can be deducted by the squared symmetry of the PCMO pattern perfectly matching that of STO substrate (Figure 4d). Therefore, the electron diffraction patterns of the STO substrate (Figure 4c) and of the PCMO film (Figure 4d) have been imaged in two different pictures.

They indicate that the following epitaxial relations are present:

- Out-of-plane: [010] PCMO || [001] STO
- In-plane: [200] PCMO || [110] STO; [101] PCMO || [010] STO

Thus, it can be concluded that the face diagonal of cubic STO unit cell is parallel to the orthorhombic base side. In Figure 4e,f, the electron diffraction patterns of the (001) PCMO film/(110) STO substrate and of the bare (001) PCMO films are shown, respectively. The principal plane distances that have been measured are 4.48 Å, 3.87 Å, 2.75 Å and 2.25 Å. They are almost the same for the two materials, and only the first value of 4.48 Å can be univocally assigned to the [110] direction of the PCMO film, while the other values have been attributed to the different directions of the STO substrate and PCMO film using the appropriate Miller indexes indicated in the two-electron diffraction images.

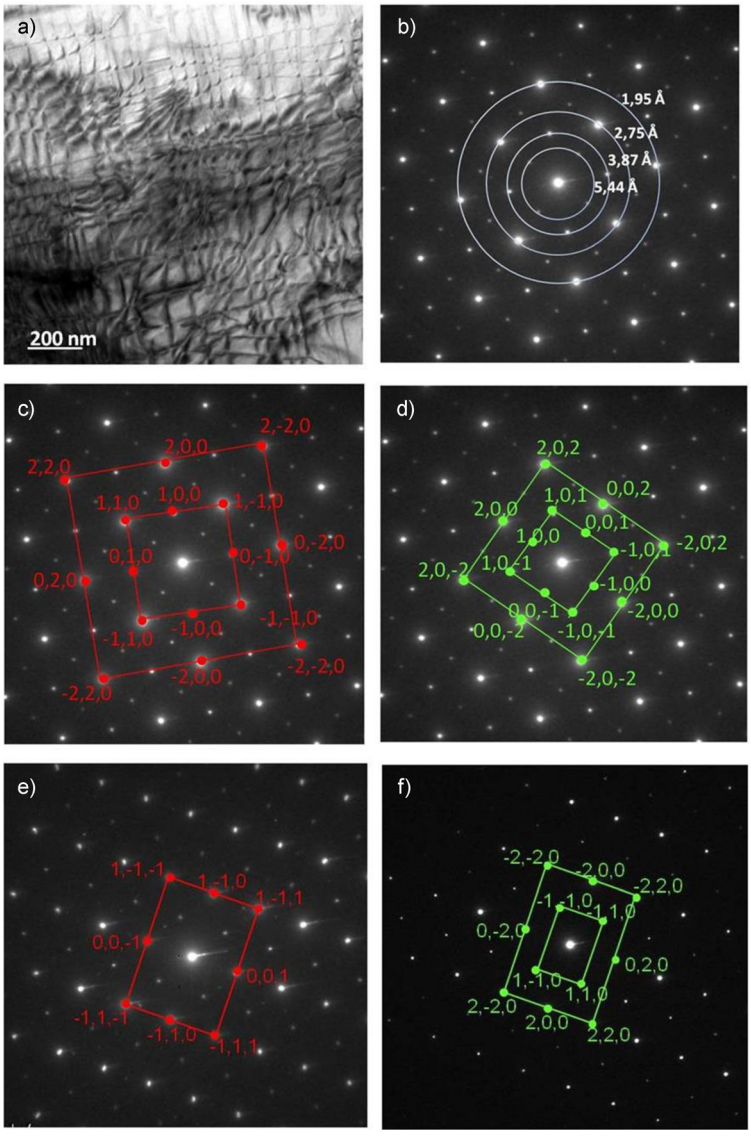

Figure 4. Transmission electron microscopy (TEM) plane view (a) and selected area electron diffraction (SAED) patterns (b) from the [001] zone axes of the PCMO thin film on STO (001). In particular, the SAED patterns from substrates STO (001) and STO (110) are highlighted as red spots and lines in panels c and e, respectively. The SAED patterns from PCMO [010] and [001] films on STO (001) and STO (110) are highlighted as green spots and lines in panels d and f, respectively.

In the case of the (001) PCMO growth on the (110) STO substrate, no rotation of its unit cell on the plane has been observed and the following epitaxial relationships can be described:

- Out-of-plane: [001] PCMO || [110] STO
- In-plane: [020] PCMO || [001] STO; [020] PCMO || [001] STO

To establish the phase purity of PCMO films, XPS analyses have been carried out on as-deposited sample and after 60 s sput-

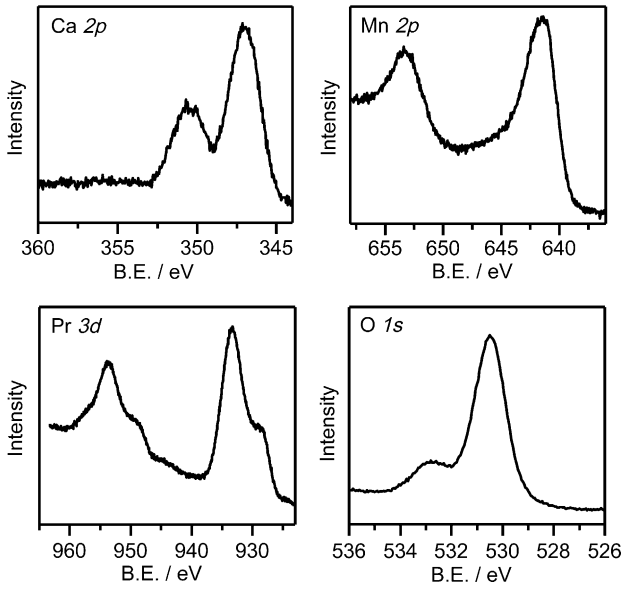

Figure 5. X-ray photoelectron spectroscopy (XPS) Ca *2p*, O *1s*, Mn *2p* and Pr *3d* spectral regions after 60 s sputtering of a PCMO film deposited on STO (001) substrate.

tering. XPS Ca *2p*, O *1s*, Mn *2p* and Pr *3d* spectral regions were acquired after 1 min of sputtering (Figure 5), performed in order to remove "adventitious" carbon and carbonates. It is worthy to note that the shape and position of Ca, Mn and Pr bands of PCMO were not significantly affected by the short sputtering. The Pr $3d_{5/2}$ band is centered at 933.5 eV pointing to a Pr^{3+} species. The shoulders observed at lower binding energy (B.E.) for Pr *3d* peaks are well-known satellite bands of Pr^{3+}, thus confirming the trivalent state of praseodymium.[39,40]

Mn $2p_{3/2}$ band is at about 641.5 eV, consistent with the Mn^{3+} and Mn^{4+} state.[41] Moreover, a more accurate indication of the valence state of manganese can be obtained from the Mn *3s* spectral region. The Mn *3s* band splitting, which originates from exchange coupling between the *3s* hole and the *3d* electrons, is the best indicator of the Mn valence state.[42,43] The observed value of 5.2 eV is consistent with a formal valence state ranging from +3.0 to +3.2. Ca $2p_{3/2}$ band is centered at 347.1 eV according to Ca^{2+} state. Band positions of all observed elements point to the PCMO formation. The XPS depth profile indicates an homogeneous composition along the film thickness up to the interface, which points to a $Pr_{0.7}Ca_{0.3}MnO_3$ stoichiometry in agreement with EDX analysis (Figure 6). Note that the C content decreases from 3–4% in the outermost part to 1–2% in the film bulk, thus indicating a low carbon contamination.

The field-emission scanning electron microscopy (FE-SEM) images of the PCMO films deposited on STO (001) and STO (110) show a uniform and homogeneous morphology. The film deposited on STO (001) shows a quite flat and uniform surface with square-shaped pinholes (Figure 7a). The effect of the different substrate orientation is evident in the morphology of PCMO films deposited on STO (110) (Figure 7b). In this case, rectangular-shaped grains of hundreds of nanometers in dimension are arranged in a textured fashion on the surface.

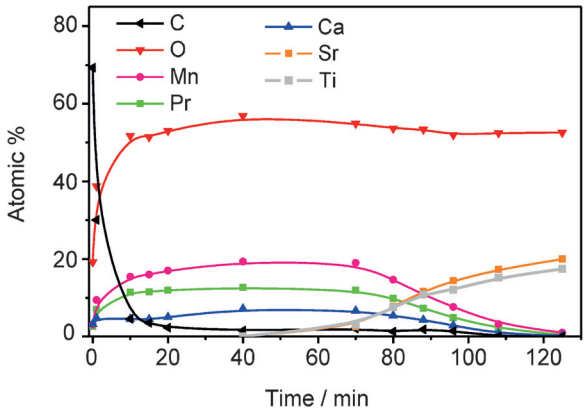

Figure 6. Depth profile of a PCMO film deposited on STO (001) substrate.

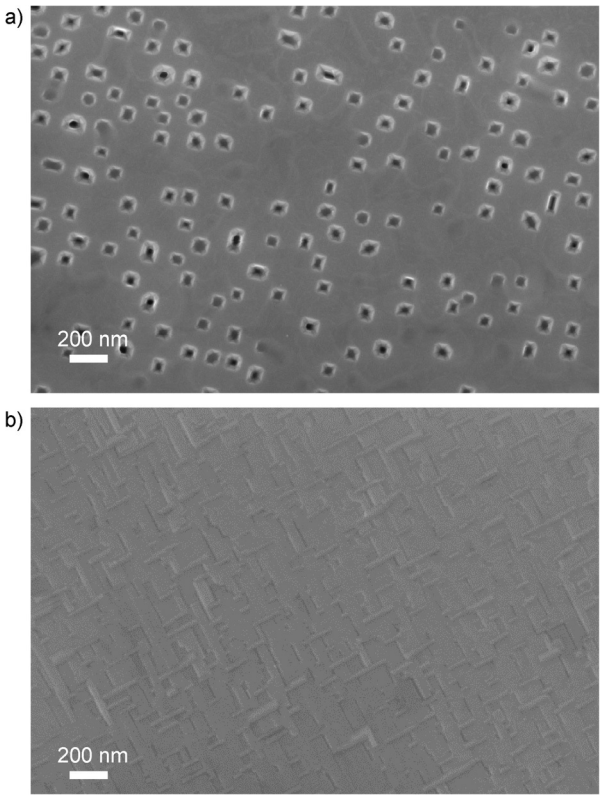

Figure 7. Secondary electron field-emission scanning electron microscopy (FE-SEM) images of PCMO films grown on a) STO (001) and b) STO (110).

Magnetic and electrical properties of PCMO films

ZFC/FC magnetic measurements have been performed on PCMO films grown on STO (001) in the range of temperature between 5 K and 300 K by applying a magnetic field parallel to the film plane. Field values of 0.5, 1, 3 and 5 T have been selected in order to explore the phase diagram of the samples as well as to evaluate the characteristic transition temperatures of each sample and their dependence on the applied magnetic field. Results obtained for the sample grown on STO (001) substrate are shown in Figure 8.

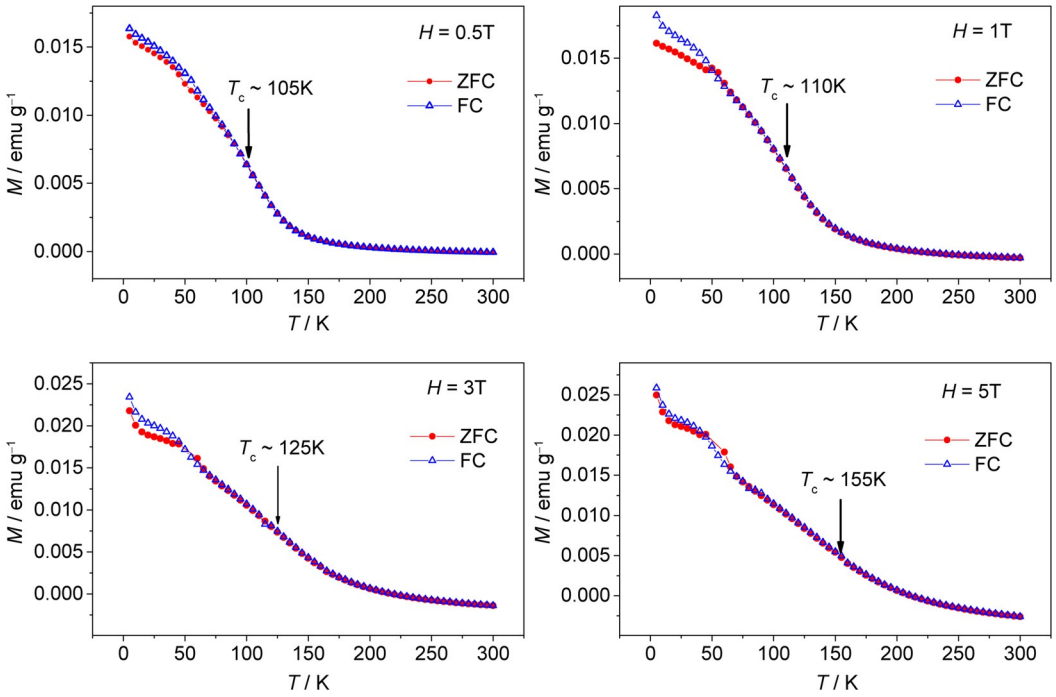

Figure 8. ZFC (●) and FC (△) curves obtained at different magnetic fields (0.5, 1, 3 and 5 T) from the sample grown on STO (001) substrate. Arrows indicate the transition temperature (T_c) determined from derivatives dM/dT.

Analysis of the FC curves reveals the presence of a FM transition, T_c, depending on applied magnetic field and raising on increasing the field.[44] All the measured samples present also a blocking temperature (T_b) of ≈50 K below which ZFC measurements show smaller magnetization values than FC ones. Both temperatures, T_c and T_b, are in agreement with literature reports[6,45] as well as with the reported phase diagram of PCMO samples,[44,46] which considers the system described as a canted antiferromagnetic structure for $T > T_c$ followed by the onset of a FM phase for $T = T_c$.

The coexistence of a canted AFM phase with an FM one also explains the observed behavior at temperatures below T_b. During the ZFC procedure, spins are not necessarily frozen aligned with the magnetic field later applied. By increasing the temperature, spins alignment with the external magnetic field becomes convenient thanks to thermal fluctuations. On the contrary, during FC procedure, spins are already frozen aligned with the field.

Transport measurements were also performed in order to establish dependences of conduction properties of the films on temperature and applied magnetic fields.In Figure 9, it is shown the temperature dependence (in absence of magnetic field and with an applied field of 6 T) of resistivity of the two halves of a sample grown on STO (001) substrate and then divided in two parts, one annealed at 800 °C in oxygen atmosphere for 2 h, the other not annealed. Both the samples present a change in the resistivity temperature dependence occurring at a temperature T_ρ close to the magnetic transition temperature found and equal to a T_ρ value of ≈115 K for the sample not annealed (Figure 9a) and 130 K for the annealed one (Figure 9c). Resistivity curves at $T < T_\rho$ show no temperature dependence. Although a change of $\rho(T)$ dependence is present, no transition to a metal phase is observed, and we can only infer an onset of such transition. At the same time, given the absence of noticeable changes in the values of resistance with the application of magnetic fields up to 6 T (with the exception of a little decrease of resistivity for temperature lower than 50 K), no CMR effect is observed. Since the transition to a metal phase is strongly related to the presence of strain effects and to the thickness of the film,[47,48] a magnetic field higher than 6 T could be needed to induce the insulant-metal transition in the studied films.

At temperatures above T_ρ, resistivity curves present an exponential-like nature. This behavior could be described[49] by Mott–Hubbard model or by thermally activated hopping (TAH) of small polarons (Holstein polarons). In the Mott–Hubbard model, resistivity can be written as in Equation (1), where ρ_∞ is the saturation resistivity (the value of resistivity for $T \to \infty$), while T_0 is related to the localization length of carriers.[50]

$$\rho_{MH}(T) = \rho_\infty \exp\left[(T_0/T)^{\frac{1}{4}}\right], \quad (1)$$

Thermally activated hopping approximation describes temperature dependence of resistivity as per Equation (2), where ρ_0 is a parameter related to hopping length of polarons and T_0 represent the polaron formation energy.[51]

$$\rho_{TAH}(T) = \rho_0 T \exp[T_0/T], \quad (2)$$

In Figure 9b, it is shown the high temperatures ($T > T_\rho$) values of ln(ρ) versus 1/T of the not annealed films together

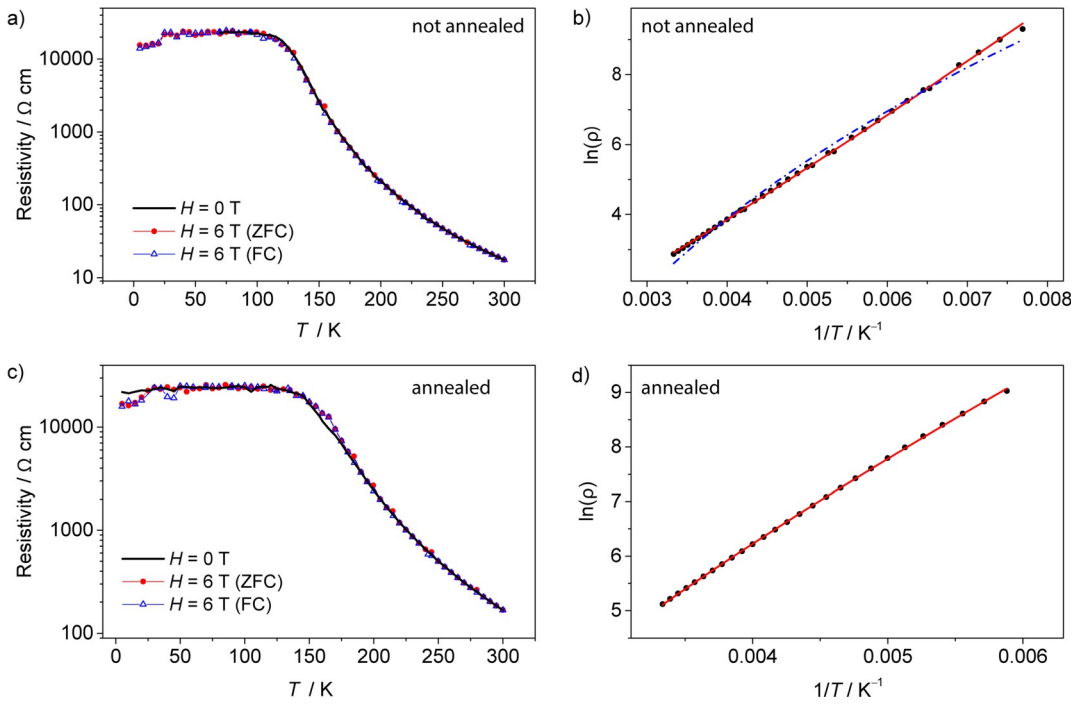

Figure 9. Resistivity versus temperature for a) not annealed and c) annealed films grown on STO (001) substrate: measurements in the absence of an external magnetic field (——); measurements in presence of a magnetic field $H = 6$ T after cooling the sample in zero field (●); resistivity measured cooling the films in presence of a magnetic field $H = 6$ T (△). b) ln(ρ) as a function of $1/T$ of the not annealed sample in zero magnetic field; best fit obtained using Mott–Hubbard model (——) and TAH model (–•–•–). d) ln(ρ) as a function of $1/T$ of the annealed sample in zero magnetic field; best fit considering model described by Equation (4) [——].

with the best fits obtained for models represented by Equations (1) and (2). Results of fits suggest that the TAH model better describes temperature dependence of resistivity of sample. Parameter values given by fit procedure are listed in Table 1. Following Jaime et al.,[52] we can express ρ_0 using Equation (3), where a is the hopping distance, x is the nominal doping level and ω_0 is the optical phonon frequency.

$$\rho_0 = \frac{a\,k_B}{x(1-x)e^2\omega_0}\,, \tag{3}$$

If we choose a ω_0 value of $\approx$1012 Hz, we can give an estimation for the hopping distance obtaining an a value of $\approx$8.4 Å, corresponding roughly to twice as the pseudocubic lattice parameter. In Figure 9d, it is shown the result of the fit performed on the annealed sample. In this case, it was not possible to determine which one of the two models better describe resistivity temperature behavior. Taking the adjusted R value as a measure for the goodness of fits, we in fact obtained for both the model a value of 0.998. This behavior hints a transition between a TAH-dominated conduction process to a MH mechanism.

Considering the electric transport governed by both mechanisms described in Equations (1) and (2) in parallel, we can represent total resistivity as shown in Equation (4).

$$\rho = \frac{\rho_{MH}\,\rho_{TAH}}{\rho_{MH} + \rho_{TAH}}\,, \tag{4}$$

The adjusted R value obtained using the model defined by Equation (4) is equal to 0.999, and the fitted curve, shown in Figure 9d, gives a better accord to experimental data. Parameters giving the best fit are listed in Table 1.

Table 1. Best-fit parameters for Mott–Hubbard and TAH models.

Conditions	ρ_∞ [Ω cm]	T_{0_HM} [K]	ρ_0 [Ω cm K^{-1}]	T_{0_TAH} [K]
Not annealed	$(1.7\pm0.8)\cdot10^{-11}$	$(1.7\pm0.1)\cdot10^{8}$	$(2.16\pm0.06)\cdot10^{-4}$	1694 ± 5
Annealed[a]	$(1.03\pm0.12)\cdot10^{-9}$	$(1.44\pm0.02)\cdot10^{8}$	$(3.83\pm0.14)\cdot10^{-3}$	1752 ± 8

[a] For the annealed sample, reported data were obtained from the model described by Equation (4).

Structure/properties relationship

A novel multi-component single-source approach has been applied to the MOCVD synthesis of PCMO on single-crystal perovskite substrate: STO (001) and STO (110). The $SrTiO_3$ substrate possesses a perovskite cubic structure with a unit cell parameter $a = 3.905$ Å, very similar to the lattice parameter of the PCMO pseudocubic structure of $a = 3.855$ Å. For this reason, the STO represents the model guide on which the perovskite structure of the PCMO can replicate. In fact, the real structure of $Pr_{0.7}Ca_{0.3}MnO_3$ is P_{nma} orthorhombic with parameters $a = 5.4646(2)$ Å, $b = 7.6749(3)$ Å, $c = 5.4308(2)$ Å.[53]

TEM data give a value of 5.44 Å for the in-plane axis of PCMO films grown on (001) STO. This represents an average value between the *a*- and *c*-axis, since it is not possible to distinguish between the two axes parameter values by means of conventional TEM measurements. The value of the *b*-axis has been estimated, from the XRD measurements, to be equal to 7.60 Å. The *a*/*c* axis data translate into a small lattice mismatch (1.5%) between film and substrate considering that the orthorhombic PCMO base side is parallel to the face diagonal of the cubic STO (001) unit cell, thus favoring the formation of epitaxial films. In the case of the films grown on STO (110), according to previously reported studies on surface-energy minimization,[54] it is likely that the PCMO (001) growth occurs against the (121) one, with one (001) oriented cell lying on two 110 STO units, with a mismatch of 1.5% and 2.5% regarding the *a*- or *c*- and *b*-axis matching with the substrate, respectively.

TEM measurements point to in-plane ordering between the film and the substrate for both orientation growth, thus even though the films are not single crystalline, an heteroepitaxial growth may be considered since the grains are perfectly triaxially aligned with respect to the substrate, that is, there is a consistent crystallographic relationship between the crystal lattice of the film grains and the substrate.[55]

Magnetic and transport measurements have shown a correlation between the onset of a ferromagnetic phase and a change of resistivity behavior that can be interpreted as precursor of a metal transition. High-temperature analysis of resistivity has shown different transport mechanisms taking place in annealed and not annealed films. Transport in the latter is well described by a thermally activated hopping model. Annealed film showed a more complex behavior; a model based on a combination of Mott–Hubbard and TAH mechanism, considered as two resistance sources in parallel, was found to describe the experimental data well. The observed transport behavior may be compared with literature reports where, depending on the characteristics of the PCMO films, Mott-like dependence of resistivity at lower temperature[21] or TAH mechanism[56] can be found. The different behavior observed by Gorbenko et al.[21] could be associated with the different deposition conditions of the two MOCVD approaches.

It is interesting to compare the data on PCMO films presented here with those reported in the literature. In particular, the comparison with bulk and nanoparticles properties[57] will add a tile in the overall characterization mosaic for the different forms of PCMO. In fact, while several studies have been carried out on the resistive switching properties of PCMO,[7–10,58] to our knowledge, this study described herein represents the first investigation of magnetic and electrical properties of PCMO films grown on STO, since previous magnetic or transport regime investigations have been predominantly carried out on PCMO ultrathin films (<10 nm),[54,59] having lattice parameters quite different from the bulk ones and, hence, the properties of these ultrathin films were due to the strain state.

Charge ordering has not been observed in our films, and this finding is in accordance with data related to the effect of grain dimensions. In the case of nanoparticles, no transition to a charge-ordered phase has been observed for nanoparticles with sizes smaller than about 100 nm, depending on the Pr/Ca ratio and applied magnetic field.[57]

Conclusion

PCMO thin films have been grown through an MOCVD process using a molten multimetal source. The epitaxial films consist of the $Pr_{0.7}Ca_{0.3}MnO_3$ pure phase, with a different microstructure and morphology depending on the used substrate. Magnetic measurements provided evidence of the presence of an FM transition temperature, which has been correlated to the transport properties of the film. Moreover, a correlation within the transport properties and the annealing of the substrate has been highlighted.

Experimental Section

The PCMO films were deposited using a mixture of $Pr(hfa)_3$·diglyme, $Ca(hfa)_2$·tetraglyme and $Mn(tmhd)_3$ precursors as sources of Mn^{3+}, Pr^{3+} and Ca^{2+}, respectively, in a low-pressure horizontal hot-wall reactor fitted with individual inlet tubes for the carrier and reaction gases. A scheme of the reactor is reported in Ref. [60]. The $Pr(hfa)_3$·diglyme and $Ca(hfa)_2$·tetraglyme adducts were synthesized as previously reported,[33,34] while $Mn(tmhd)_3$ was purchased from Strem Chemicals Inc. (Bischheim, France). and used as received. The single multicomponent source with a 1.8:0.6:1 stoichiometric ratio was loaded inside the reactor in an Al_2O_3 boat located in the vaporization zone and resistively heated at the appropriate vaporization temperature (130 °C). The vaporized source materials were transported by a 150 sccm (standard cubic centimeters per minute) Ar gas flow to the deposition zone. Water-saturated oxygen flow (900 sccm) was used as the reaction gas to avoid any F contamination. Depositions were conducted for 60 min at a deposition temperature of 900 °C yielding films 250 nm thick. The depositions were performed on $SrTiO_3$ (001) and $SrTiO_3$ (110). Single crystals of STO were taken from routine batches prepared by Crystal GmbH (Berlin, Germany).

Thermogravimetric (TG) analysis: Measurements of the mixture precursors were performed using a Mettler Toledo SDTA 851e TG analyzer. Thermal investigations were carried out at 760 torr under purified N_2 flow, fed into the working chamber at 30 sccm. The heating rate was 5 °C min^{-1}. Measurements were run from 25 to 350 °C with an accuracy of ± 0.1 °C. Sample weights used were about 8 mg for TG analysis and 15 ± 1 mg for isothermal TG measurements.

Structural and morphological characterization: θ–2θ XRD patterns and ω-scan rocking curves were recorded on a θ–θ Bruker D5005 diffractometer using a Göbel mirror to parallel the Cu K_α radiation operating at 40 kV and 30 mA. In-plane TEM analyses were performed using a Hitachi S4500 FE microscope, and morphologies were examined using a field-emission scanning electron microscope ZEISS SUPRA VP 55.

Chemical composition: The films were analyzed by EDX analysis using an INCA-Oxford windowless detector. XPS was measured at 45° take-off angles relative to the surface plane with a PHI 5600 multitechnique system (base pressure of the main chamber: 3×10^{-10} Torr). Samples were excited with the Al-Kα radiation, and XPS peak intensities were obtained after a Shirley background removal. Spectra calibration was achieved by fixing the "adventitious" C *1s* peak at 285.0 eV. Depth profiles were obtained by alternating XPS

analysis and Ar^+ sputtering, carried out in a $3\times3\ mm^2$ area (3 kV, beam current 1.0 μA).

Magnetic analysis: Measurements to determine the temperature dependence of ZFC and FC magnetization were carried out on an MPMS superconducting quantum interference device (SQUID) magnetometer from Quantum Design Inc. (San Diego, CA, USA. The measurements were performed in the temperature range 5–300 K and in 0.5, 1, 3 and 5 T dc magnetic fields applied parallel to the film plane.

Transport analysis: Measurements were carried out in a PPMS system from Quantum Design Inc., by using the dc four-probe method making flow current in the films plane and parallel to the applied magnetic field. Electric contacts on the samples were made using silver paint on gold pads previously evaporated on the films. Measurements were collected in the temperature range 5–300 K and with magnetic fields up to 6 T.

Acknowledgements

The authors thank the Italian Ministry of Education, Universities and Research (MIUR) for financial support through grants PRIN 2009 N, 20097X44S7_002 and ERC 2010-AdG267746, MolNanoMaS.

Keywords: ferromagnetism · manganites · metal-organic chemical vapor deposition (MOCVD) · perovskites · thin films

[1] J. M. D. Coey, M. Viret, S. von Molnár, *Adv. Phys.* **2009**, *58*, 571 – 697.
[2] S. Jin, T. H. Tiefel, M. McCormack, R. A. Fastnacht, R. Ramesh, L. H. Chen, *Science* **1994**, *264*, 413 – 415.
[3] S. Q. Liu, N. J. Wu, A. Ignatiev, *Appl. Phys. Lett.* **2000**, *76*, 2749 – 2751.
[4] Y. Murakami, H. Kasai, J. J. Kim, S. Mamishin, D. Shindo, S. Mori, A. Tonomura, *Nat. Nanotechnol.* **2010**, *5*, 37 – 41.
[5] C. Zener, *Phys. Rev.* **1951**, *82*, 403 – 405.
[6] Z. Jirák, S. Krupička, Z. Šimša, M. Dlouhá, S. Vratislav, *J. Magn. Magn. Mater.* **1985**, *53*, 153 – 166.
[7] M. R. Lees, J. Barratt, G. Balakrishnan, D. M. Paul, M. Yethiraj, *Phys. Rev. B* **1995**, *52*, R14303 – R14307.
[8] a) X. Chen, N. J. Wu, J. Strozier, A. Ignatiev, *Appl. Phys. Lett.* **2005**, *87*, 233506; b) H. B. Moon, M. K. Seo, J. H. Cho, J. S. Ahn, *J. Korean Phys. Soc.* **2006**, *49*, S633 – S637.
[9] R. Waser, M. Aono, *Nat. Mater.* **2007**, *6*, 833 – 840.
[10] A. Sawa, *Mater. Today* **2008**, *11*, 28 – 36.
[11] F. Borgatti, C. Park, A. Herpers, F. Offi, R. Egoavil, Y. Yamashita, A. Yang, M. Kobata, K. Kobayashi, J. Verbeeck, G. Panaccione, R. Dittmann, *Nanoscale* **2013**, *5*, 3954 – 3960.
[12] A. Herpers, C. Lenser, C. Park, F. Offi, F. Borgatti, G. Panaccione, S. Menzel, R. Waser, R. Dittmann, *Adv. Mater.* **2014**, *26*, 2730 – 2735.
[13] K. Inoue, K. Hamaguchi, (Sharp Kabushiki Kaisha, Osaka, Japan), Eur. Pat. Appl., EP 1376598 A1, **2004**.
[14] *Chemical Vapour Deposition: Precursors, Processes, Applications*, (Eds.: A. C. Jones, M. L. Hitchman), Royal Society of Chemistry, Cambridge (UK), **2009**, Chapters 1 and 5.
[15] R. Lo Nigro, R. G. Toro, G. Malandrino, I. L. Fragalà, M. Losurdo, M. M. Giangregorio, G. Bruno, V. Raineri, P. Fiorenza, *J. Phys. Chem. B* **2006**, *110*, 17460 – 17467.
[16] G. Malandrino, L. M. S. Perdicaro, G. Condorelli, I. L. Fragala, A. Cassinese, M. Barra, *J. Mater. Chem.* **2005**, *15*, 4718 – 4722.
[17] a) J. H. Cho, C. H. Kim, Y. H. Jang, J. H. Cho, H. B. Moon, J. W. Kim, *J. Korean Phys. Soc.* **2009**, *55*, 780 – 784; b) A. Antonakos, M. Filippi, G. H. Aydogdu, W. Prellier, H.-U. Habermeier, E. Liarokapis, *Phys. Status Solidi B* **2009**, *246*, 635 – 642; c) X. Liu, I. Kim, M. Siddik, S. Md. Sadaf, K. P. Biju, S. Park, H. Hwang, *J. Korean Phys. Soc.* **2011**, *59*, 497 – 500; d) M. Fujimotow, H. Koyama, Y. Nishi, T. Suzuki, S. Kobayashi, Y. Tamai, N. Awaya, *J. Am. Ceram. Soc.* **2007**, *90*, 2205 – 2209.
[18] A. Maniwa, K. Okano, I. Ohkubo, H. Kumigashira, M. Oshima, M. Lippmaa, M. Kawasakic, H. Koinuma, *J. Magn. Magn. Mater.* **2007**, *310*, 2237 – 2238.
[19] a) M. Yamada, O. Sakai, T. Nakamura, *Thin Solid Films* **2014**, *571*, 597 – 600; b) L. Bi, S. C. Pandey, N. Ramaswamy, *Appl. Phys. Lett.* **2013**, *103*, 033516; c) S. Joo, J. Sok, *J. Korean Phys. Soc.* **2008**, *53*, 3427 – 3430.
[20] a) T. Nakamura, K. Homma, T. Yakushiji, R. Tai, A. Nishio, K. Tachibana, *Surf. Coat. Technol.* **2007**, *201*, 9275 – 9278; b) T. Nakamura, K. Homma, K. Tachibana, *J. Nanosci. Nanotechnol.* **2011**, *11*, 8408 – 8411; c) T. Nakamura, R. Tai, K. Tachibana, *J. Appl. Phys.* **2006**, *99*, 08Q302.
[21] O.Yu. Gorbenko, A. R. Kaul, A. A. Bosak, I. E. Graboy, H. W. Zandbergen, V. L. Svetchnikov, N. A. Babushkina, L. M. Belova, K. I. Kugel, *Solid State Commun.* **2000**, *114*, 407 – 412.
[22] a) O. Yu Gorbenko, A. R. Kaul, A. A. Kamenev, O. V. Melnikov, I. E. Graboy, N. A. Babushkina, A. N. Taldenkov, A. V. Inyushkin, *J. Cryst. Growth* **2005**, *275*, e2453 – e2458; b) Y. P. Sukhorukov, N. N. Loshkareva, E. A. Gan'shina, A. R. Kaul, O. Yu Gorbenko, E. V. Mostovshchikova, A. V. Telegin, A. N. Vinogradov, I. K. Rodin, *Phys. Solid State* **2004**, *46*, 1241 – 1251; c) A. M. Aliev, A. G. Gamzatov, I. K. Kamilov, A. R. Kaul, V. S. Kalitka, N. A. Babushkina, *Phys. Solid State* **2013**, *55*, 1170 – 1174.
[23] G. J. Snyder, R. Hiskes, S. DiCarolis, M. R. Beasley, T. H. Geballe, *Phys. Rev. B* **1996**, *53*, 14434 – 14444.
[24] L. Meda, K.-H. Dahmen, S. Hayek, H. Garmestani, *J. Cryst. Growth* **2004**, *263*, 185 – 191.
[25] C. Dubourdieu, M. Rosina, M. Audier, F. Wiess, J. P. Senateur, E. Dooryhee, L. Hodeau, *Thin Solid Films* **2001**, *400*, 81 – 84.
[26] S. Balevičius, P. Cimmperman, V. Petrauskas, V. Stankevič, E. E. Tornau, N. Žurauskienė, A. Abrutis, V. Plaušinaitienė, M. Sawicki, T. Dietl, M. Aleszkiewicz, *Thin Solid Films* **2006**, *515*, 691 – 694.
[27] R. G. Toro, G. Malandrino, L. M. S. Perdicaro, D. M. R. Fiorito, A. Andreone, G. Lamura, I. L. Fragalà, *Chem. Vap. Deposition* **2010**, *16*, 143 – 150.
[28] R. G. Toro, D. M. R. Fiorito, M. E. Fragalà, A. Barbucci, M. P. Carpanese, G. Malandrino, *Mater. Chem. Phys.* **2010**, *124*, 1015 – 1021.
[29] H. W. Zandbergen, J. Jansen, S. Freisem, T. Nojima, J. Aarts, *Phil. Mag.A: Phys. Cond. Matter.* **2000**, *80*, 337 – 350.
[30] K. H. Bhavsar, U. S. Joshi, *Solid State Phen.* **2013**, *209*, 198 – 202.
[31] G. Gao, S. Jin, W. Wu, *Appl. Phys. Lett.* **2007**, *90*, 012509.
[32] A. de Andrés, J. Rubio, G. Castro, S. Taboada, J. L. Martinez, J. M. Colino, *Appl. Phys. Lett.* **2003**, *83*, 713 – 715.
[33] R. Lo Nigro, R. G. Toro, G. Malandrino, I. L. Fragalà, P. Rossi, P. Dapporto, *J. Electrochem. Soc.* **2004**, *151*, F206 – F213.
[34] G. Malandrino, F. Castelli, I. L. Fragalà, *Inorg. Chim. Acta* **1994**, *224*, 203 – 207.
[35] Z. Lipani, M. R. Catalano, P. Rossi, P. Paoli, G. Malandrino, *Chem. Vap. Deposition* **2013**, *19*, 22 – 28.
[36] N° 071-5290, International Centre for Diffraction Data (ICDD), Newtown Square, PA (USA).
[37] N° 035-734, International Centre for Diffraction Data (ICDD), Newtown Square, PA (USA).
[38] A. Herpers, K. J. O'Shea, D. A. MacLaren, M. Noyong, B. Rösgen, U. Simon, R. Dittmann, *APL Mater.* **2014**, *2*, 106106.
[39] R. Lo Nigro, R. G. Toro, G. Malandrino, G. G. Condorelli, V. Raineri, I. L. Fragalà, *Adv. Funct. Mater.* **2005**, *15*, 838 – 845.
[40] H. Ogasawara, A. Kotani, R. Potze, G. A. Sawatzky, B. T. Thole, *Phys. Rev. B* **1991**, *44*, 5465 – 5469.
[41] S. Majumdar, H. Huhtinen, S. Granroth, P. Paturi, *J. Phys. Condens. Matter* **2012**, *24*, 206002.
[42] V. R. Galakhov, M. Demeter, S. Bartkowski, M. Neumann, N. A. Ovechkina, E. Z. Kurmaev, N. I. Lobachevskaya, Ya. M. Mukovskii, J. Mitchell, D. L. Ederer, *Phys. Rev. B* **2002**, *65*, 113102.
[43] M. Fujiwara, T. Matsushita, S. Ikeda, *J. Electron Spectrosc. Relat. Phenom.* **1995**, *74*, 201 – 206.
[44] D. I. Khomskii, G. A. Sawatzky, *Solid State Commun.* **1997**, *102*, 87 – 99.
[45] D. E. Cox, P. G. Radaelli, M. Marezio, S.-W. Cheong, *Phys. Rev. B* **1998**, *57*, 3305 – 3314.
[46] H. Yoshizawa, H. Kawano, Y. Tomioka, Y. Tokura, *Phys. Rev. B* **1995**, *52*, R13145 – R13148.
[47] A.-M. Haghiri-Gosnet, J.-P. Renard, *J. Phys. D* **2003**, *36*, R127 – R150.

[48] D. K. Baisnab, T. G. Kumary, A. T. Satya, A. Mani, J. Janaki, R. Nithya, L. S. Vaidhyanathan, M. P. Janawadkar, A. Bharathi, *J. Magn. Magn. Mater.* **2011**, *323*, 2823 – 2827.
[49] M. Ziese, C. Srinitiwarawong, *Phys. Rev. B* **1998**, *58*, 11519 – 11525.
[50] N. F. Mott, *Conduction in Non-Crystalline Materials*, Clarendon Press, Oxford, **1993**, p. 17 ff.
[51] I. G. Austin, N. F. Mott, *Adv. Phys.* **1969**, *18*, 41 – 102.
[52] M. Jaime, M. B. Salamon, M. Rubinstein, R. E. Treece, J. S. Horwitz, D. B. Chrisey, *Phys. Rev. B* **1996**, *54*, 11914 – 11917.
[53] P. G. Radaelli, G. Iannone, M. Marezio, H. Y. Hwang, S.-W. Cheong, J. D. Jorgensen, D. N. Argyriou, *Phys. Rev. B* **1997**, *56*, 8265 – 8276.
[54] A. Geddo Lehmann, F. Congiu, N. Lampis, F. Miletto Granozio, P. Perna, M. Radovic, U. Scotti di Uccio, *Phys. Rev. B* **2010**, *82*, 014415.
[55] E. S. Machlin, *Materials Science in Microelectronics I: The Relationships Between Thin Film and Processing and Structure*, Giro Press, Croton-on-Hudson, **1995**, p. 15 ff.
[56] H. B. Moon, S. H. Bang, O. S. Han, J. H. Cho, J. S. Ahn, *J. Korean Phys. Soc.* **2006**, *49*, S629 – S632.
[57] T. Zhang, X. P. Wang, Q. F. Fang, X. G. Li, *Appl. Phys. Rev.* **2014**, *1*, 031302.
[58] H. S. Lee, S. G. Choi, H.-H. Park, M. J. Rozenberg, *Sci. Rep.* **2013**, *3*, 1704.
[59] C. Barone, A. Galdi, N. Lampis, L. Maritato, F. Miletto Granozio, S. Pagano, P. Perna, M. Radovic, U. Scotti di Uccio, *Phys. Rev. B* **2009**, *80*, 115128.
[60] R. Lo Nigro, R. G. Toro, G. Malandrino, I. L. Fragala, *J. Mater. Chem.* **2005**, *15*, 2328 – 2337.

Received: February 5, 2015
Published online on June 5, 2015

